ELSEVIER

Journal of Fluids and Structures 19 (2004) 1–16

JOURNAL OF FLUIDS AND STRUCTURES

www.elsevier.nl/locate/jnlabr/yjfls

Experiments on heave/pitch limit-cycle oscillations of a supercritical airfoil close to the transonic dip

G. Dietz*, G. Schewe, H. Mai

Institut für Aeroelastik des DLR, Bunsenstraße 10, D-37073 Göttingen, Germany

Received 10 February 2003; accepted 28 July 2003

Abstract

Recent results from flutter experiments of the supercritical airfoil NLR 7301 at flow conditions near the transonic dip are presented. The airfoil was mounted with two degrees of freedom in an adaptive solid-wall wind tunnel, and boundary-layer transition was tripped. Two limit-cycle oscillation (LCO) test cases obtained in an adaptive test-section are proposed for comparison with numerical simulations. The results link the global aerodynamic force behavior to the observed LCOs and the identified transonic dip. The time lag of the lift response to the pitching motion of the airfoil appears to be responsible for the characteristic shape of the transonic dip. The amplitude limitation of the LCOs results from a slightly nonlinear dependency of lift and moment on the amplitude of the airfoil motion. LCOs can be controlled by relatively small forces, but amplitudes strongly depend on the damping of the aeroelastic system.

1. Introduction

The aeroelastic interaction of a typical transport-aircraft structure and the transonic flow exhibits two well-known phenomena: firstly, in the "transonic dip" (Tijdeman, 1977) the flutter speed shows a noticeable minimum between the critical Mach number where local supersonic regions occur in the flowfield and the Mach number where massive flow separation limits the operational flight regime; secondly, amplitude-limited oscillations of the structure, so-called limit-cycle oscillations (LCO), may occur (Edwards, 1996) instead of "classical" flutter where the amplitude of the structural oscillations grow exponentially at flight speeds above the critical flutter speed. It is assumed in the literature that both phenomena are linked to the inherently nonlinear aerodynamics at transonic speeds (Bendiksen, 1992). Since the relative flow speeds are close to the speed of sound, shock waves occur which may interact with the boundary layer eventually leading to flow separation. All of these mutual interactions are sources of nonlinearities. However, the aerodynamic phenomena, whose interactions are in particular responsible for the occurrence of the transonic dip as well as the amplitude limitation of the LCOs, have not yet completely been identified.

The physical understanding of the transonic dip and the LCO is of technical interest as a fundamental of an accurate prediction since the avoidance of transonic flutter is a key aircraft design problem (Edwards et al., 1983). Furthermore, LCOs might be used to extend the operational flight regime, although they are usually seen as undesirable vibrations that limit the aircraft functionality (Meijer and Cunningham, 1992). One could imagine flying in an unstable regime by using an active damping system, with the stable LCO as a fall-back position if the damping system fails. Obviously the amplitudes of the LCO have to be sufficiently small so that the structure does not fail by exceeding its ultimate load limit. Thus, LCOs could degrade the safety problem, as in the case of classical flutter, into a fatigue problem. In any case, reliable prediction methods for flutter at transonic speeds are needed, and the physics of transonic flutter must be understood, in order for the modelling to be robust and accurate. Thus, nonlinear aeroelasticity of large aspect-ratio

*Corresponding author.
E-mail address: guido.dietz@dlr.de (G. Dietz).

0889-9746/$ - see front matter
doi:10.1016/j.jfluidstructs.2003.07.019

wings is the subject of recent and current investigations. The present study concentrates on two spatial dimensions since a heaving and pitching airfoil can be seen as a representative section of a wing exhibiting bending and torsional oscillations.

Experimental investigations on nonclassical aeroelastic instability and response phenomena have been rare. Wind-tunnel test results of a NACA 0012 airfoil single-side mounted with two degree of freedom were published within the Benchmark Models Program at NASA Langley by Rivera et al. (1991, 1992). A conventional flutter boundary showing a transonic dip, a plunge instability region and stall flutter was found. Moreover, unsteady pressure measurements at the conventional flutter boundary were presented. One time-series of a combined heave and pitch motion exhibiting an LCO behavior at transonic flow conditions was shown (Rivera et al., 1991), but the amplitudes of the motion were not scaled. Edwards et al. (2001) measured flutter boundaries and LCO behavior of a semi-span business jet wing-fuselage model MAVRIC-I. The influence of the dynamic pressure and the angle of attack on the LCO behavior was reported by showing maps of the signal amplitude of wingtip accelerometers depending on the inflow Mach number and dynamic pressure. Furthermore, unsteady pressure distributions were measured at three span positions. The data set provides code validation test cases but for a more or less complex configuration. To the best of our knowledge, the first heave/pitch LCOs of a two-side mounted supercritical rigid airfoil in transonic flow were observed by Schewe and Deyhle (1996) in their exploratory experiment with an airfoil model shaped as NLR 7301. Similar data obtained in the same test set-up [Knipfer and Schewe (1999); corrected structural-dynamic parameters in Schewe et al. (2003)] are still subject of numerical investigations.

Numerical studies of nonclassical flutter in transonic flow have been performed based on various numerical CFD and CSM models. Bendiksen (1992) studied the influence of shock dynamics on flutter and divergence in transonic flow by integrating the Euler equations whilst neglecting the structural damping. Nonlinear aeroelastic phenomena such as LCOs, weak divergence as well as flutter-divergence interactions were observed and described. However, similar to Schulze (1997) the reported simulated LCO amplitudes were quite high. Bendiksen (1992) partially discussed the transonic flutter behavior on the basis of the fluid–structure energy exchange: he observed that in transonic flow the phase difference between heave and pitch motion tends to adjust such that single-degree-of-freedom (sdof) flutter occurs. Bendiksen (1992) argued that the averaged power per cycle contributed by the lift due to the shock motion is maximized in this case. Morton and Beran (1999) investigated numerically the pitch-and-plunge flutter of a rigid NACA 64A006 airfoil in inviscid transonic flow. Although the predictions of flutter onset with three independent aeroelastic codes based on Euler equations were in agreement, the simulated LCO amplitudes differed noticeably. They speculated that differences in the numerical dissipation and the applied time steps caused the discrepancies. Weber et al. (2001) as well as Tang et al. (2003) computed LCOs of the NLR 7301 by integrating the thin-layer Navier–Stokes equations within their CFD model. These authors tried to simulate the experimental test case MP77 proposed by Knipfer and Schewe (1999). They tested different turbulence models, but the computed LCO amplitudes were an order of magnitude higher than the measured ones. Weber et al. (2001) suspected that, in part, the discrepancy was due to the neglected wind-tunnel interference. Thus, Castro et al. (2001) continued the work of Weber et al. (2001), taking into account the presence of the porous wind-tunnel walls. It was shown that modelling the wind-tunnel wall porosity significantly affects the LCO behavior. The simulated LCO amplitudes were also quite sensitive to the porosity parameter, whereas the flutter frequency as well as the phase difference between the pitch and the heave motion remained nearly constant. The numerical investigation indicated that wind-tunnel walls strongly influence the flutter characteristics compared with free-flight conditions. Nevertheless, with a wall porosity between 12% and 16% instead of 6% in the experiment, the predicted LCO amplitudes were comparable with the measured ones. The results confirmed the authors' previous decision to avoid this additional challenge in simulation by providing well-defined boundary conditions, using an adaptive test-section (Wedemeyer et al., 1998) for the experiments reported here. Thomas et al. (2002) investigated numerically the LCO behavior of the NLR 7301 in the vicinity of MP77 using a harmonic balance approach. Assuming inviscid flow led to nearly linear aeroelastic behavior while the LCOs in viscous flow exhibited high amplitudes that are comparable with Weber et al. (2001) and Tang et al. (2003). However, the effects of viscosity play an important role in correct modelling of the LCO response phenomena (Thomas et al., 2002). Beside the importance of damping in the accurate prediction of LCOs, Meijer and Cunningham (1992) showed by means of a semi-empirical LCO prediction method that the time lag of the aerodynamic response to the structural motion strongly affects the LCO eigenmode.

Here, we report recent results from experiments on heave/pitch limit-cycle oscillations of the supercritical airfoil NLR 7301 with tripped boundary-layer transition at flow conditions close to the transonic dip. The measurements were carried out in the adaptive test-section of the TWG Göttingen. From these data, two additional LCO test cases together with the geometric boundary conditions of the adaptive test-section are proposed as a complement to Schewe et al. (2003) MP77. The experimental results link the global aerodynamic force behavior to the observed LCOs and the detected transonic dip. It is shown which global aerodynamic force behavior is responsible for the transonic dip and for the amplitude limitation of the LCOs. Furthermore, the influence parameters on the amplitude of LCOs are discussed.

2. Test set-up

Only those details regarding the set-up and the test procedure that are important in order to understand the reported results are presented here. More detailed information may be found in Schewe et al. (2002).

The experiments were conducted in the Transonic Wind tunnel Göttingen (TWG). The TWG is a continuously working facility with a 1 m × 1 m adaptive test-section. The ratio of the tunnel height to the chord of the investigated airfoil models is 3.333. Therefore the top and bottom walls were adapted to the stationary flow at the mean angle of attack of the airfoil, where the static aeroelastic equation is satisfied. The wall interference is minimized by a one-step method of wall adaptation based on a Cauchy-type integral (Wedemeyer et al., 1998). The displacement thickness of the turbulent wind-tunnel wall boundary layer is predicted by Head's method (Cebeci and Bradshaw, 1979) and is added to the wall shapes; top and bottom wall displacement thicknesses are obtained according to the measured pressure gradients at each wall while the gradient is neglected for the sidewalls (Jacobs, 2002). This adaptation to the mean steady position of the airfoil yields nearly a minimum residual wall interference for a moderately oscillating airfoil, as shown in pretests (Jacobs, 2002). The applied wall shapes may be used in numerical simulations since they are listed in Table 2 for the proposed LCO test cases. The lowest value for the wind-tunnel resonance frequency can be estimated using the method of Voß (1998): the ratio of flutter frequency to wind-tunnel resonance frequency is smaller than 35% for the reported data.

Two set-ups were employed to obtain the presented results. One set-up allows free heave and pitch motions of the airfoil for flutter tests. A theoretical model representing the structural dynamics of this set-up is described in Section 3. The same set-up also was used for forced harmonic heave oscillations of the airfoil with a blocked pitch motion and hydraulic actuators in the heave direction. The other set-up forces harmonic pitch oscillations of the airfoil by means of hydraulic rotation cylinders. In both set-ups, the airfoil is mounted on each side to a piezoelectric balance of high stiffness (Schewe, 1991) in order to measure the steady and unsteady loads lift, drag and pitching moment. Two laser triangulators on each side of the wind tunnel measure the instantaneous heave and pitch of the model. For the flutter-test set-up a control system has been developed to introduce forces in heave direction which are measured piezoelectrically. A digital signal processor (DSP) device derives the heave velocity from the laser-triangulator signals such that a voltage proportional to this velocity can be passed into one electrodynamical exciter on each side. Small heave motions of the airfoil can then either be amplified or, by applying the inverted signal, damped. Tests revealed that in open-loop state this flutter control system can be seen as nonintrusive.

Two airfoil models were shaped as the supercritical NLR 7301 airfoil with the contour given by Zwaan (1979) except that this geometry was cut off at $x/c = 1$. Thus, the trailing edges of the models are blunt with approximately 0.1% chord. In the present investigation the chords meet the leading and trailing edges of the models so that the given angle-of-attack α differs from the NLR results by $\alpha = \alpha_{\mathrm{NLR}} - 0.183^\circ$. Both models are made of a carbon-fiber composite structure having a chord of $c^* = 0.3$ m and a span of $b^* = 1$ m. They are light weight, very stiff and may be assumed to be rigid. In order to investigate the flow around a forced oscillating airfoil, one model is equipped with 64 miniature pressure transducers measuring both steady and unsteady pressure differences. These sensors are arranged beneath the model surface and the pressure taps are located in a zig-zag pattern of $\pm 0.5\%$ span around the middle section at 50% span. Laminar-turbulent boundary-layer transition has been tripped at 7% chord on the suction and 14% chord on the pressure side by zig-zag tape with a height of 0.0467% chord. The effectiveness of the transition tripping has been checked by infrared imaging. The tripping has been applied in the attempt of obtaining a better comparison with numerical simulations, since the accurate prediction of the transition region is still an unsolved problem, in particular for unsteady flows.

3. Equations of motion

The heave and pitch motions of the rigid airfoil in the flutter-test set-up are modelled by a two-degree-of-freedom system as shown in Fig. 1. The corresponding equations of motion can be written in nondimensional form as

$$v_\infty^2 \mathbf{M} \frac{\partial^2 \mathbf{u}(t)}{\partial t^2} + 2 v_\infty \mathbf{D} \frac{\partial \mathbf{u}(t)}{\partial t} + \mathbf{K}\mathbf{u}(t) = \frac{2}{\pi} \frac{v_\infty^2}{\mu} \mathbf{f}(t), \tag{1}$$

where

$$\mathbf{M} = \begin{bmatrix} 1 & -x_\alpha \\ -x_\alpha & r_\alpha^2 \end{bmatrix}, \quad \mathbf{D} = \begin{bmatrix} \delta_h \omega_h/\omega_\alpha & 0 \\ 0 & \delta_\alpha r_\alpha^2 \end{bmatrix}, \quad \mathbf{K} = \begin{bmatrix} (\omega_h/\omega_\alpha)^2 & 0 \\ 0 & r_\alpha^2 \end{bmatrix},$$

$$\mathbf{f}(t) = \begin{bmatrix} c_l(t) \\ c_m(t) + x_0 c_l(t) \end{bmatrix} \quad \text{and} \quad \mathbf{u}(t) = \begin{bmatrix} h(t) \\ \alpha(t) - \alpha_0 \end{bmatrix}.$$

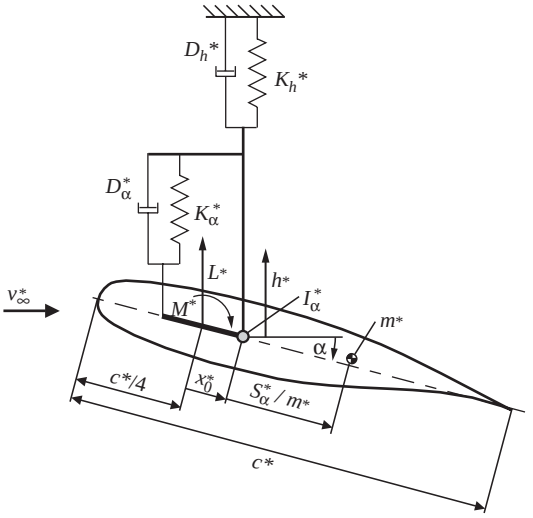

Fig. 1. Schematic of the structural model.

Eq. (1) describes the motion of the airfoil, its nondimensional heave $h(t) = h^*(t)/c^*$ at the elastic axis as well as the difference between its angle of attack $\alpha(t)$ and its off-wind value α_0 in the nondimensional time $t = t^* v_\infty^*/c^*$. With the dimensional quantities chord length c^*, mass m^*, static mass moment S_α^*, mass moment of inertia I_α^*, spring constants $K_{\alpha/h}^*$ and damping coefficients $D_{\alpha/h}^*$ as well as the free-stream speed v_∞^* and density ρ_∞^* the structural-dynamic parameters are made nondimensional as follows:

$$\text{elastic axis to 1/4-chord point distance}: x_0 = x_0^*/c^* = 0.0,$$

$$\text{elastic axis to center of mass distance}: x_\alpha = S_\alpha^*/(m^* c^*) = 0.0420,$$

$$\text{radius of gyration about the elastic axis}: r_\alpha = \sqrt{I_\alpha^*/(m^* c^{*2})} = 0.1828,$$

$$\text{Lehr's pitch-damping coefficient}: \delta_\alpha = D_\alpha^*/\left(2\sqrt{K_\alpha^* I_\alpha^*}\right) = 0.15\%,$$

$$\text{Lehr's plunge-damping coefficient}: \delta_h = D_h^*/\left(2\sqrt{K_h^* m^*}\right) = 0.43\%,$$

$$\text{uncoupled natural frequency ratio}: \omega_h/\omega_\alpha = \sqrt{K_h^*/m^*}/\sqrt{K_\alpha^*/I_\alpha^*} = 0.6991. \quad (2)$$

The aerodynamic loads lift $L^*(t)$ and pitching moment $M^*(t)$ that act on the airfoil with span b^* through the 1/4-chord point can be nondimensionalized as

$$\text{lift coefficient}: c_l(t) = L^*(t)/\left(\frac{\rho_\infty^*}{2} v_\infty^{*2} c^* b^*\right),$$

$$\text{moment coefficient}: c_m(t) = M^*(t)/\left(\frac{\rho_\infty^*}{2} v_\infty^{*2} c^{*2} b^*\right). \quad (3)$$

The reciprocal of the reduced natural pitching frequency $k_\alpha = \sqrt{K_\alpha^*/I_\alpha^*}\, c^*/v_\infty^* = 86.95\ \text{m/s}/v_\infty^*$ can be interpreted as a nondimensional free-stream speed $v_\infty = 1/k_\alpha$ and is called the reduced speed. The mass ratio $\mu = (m^*/(\pi/4 c^{*2} b^*))/\rho_\infty^* = 371.62\ \text{kg/m}^3/\rho_\infty^*$ describes the ratio of the structural inertial forces to the aerodynamic loads, whereas the flutter index $\text{fi} = 2v_\infty/\sqrt{\mu}$ characterizes the ratio of the aerodynamic loads to the elastic forces.

3.1. Structural-dynamic parameters

Eqs. (2) present the structural-dynamic parameters of the flutter-test set-up. The parameters, chord length, mass and torsional-spring constant, were measured directly. The mass moment of inertia, the static mass moment and the

bending-spring constant were measured and then corrected by the results of a ground vibration test (GVT). The correction procedure minimizes the discrepancies between the theoretically obtained eigenfrequencies and maximizes the collinearity of the eigenvectors to the values that were measured. The relative difference between the eigenfrequencies of the structural model without aerodynamic loads to those of the ground vibration test are smaller than 0.3%, the collinearity of the eigenvectors is greater than 99.7%. The relative error of the measured eigenfrequencies is very small whereas the damping constants may be obtained from the GVT with a relative error of $\mathcal{O}$ (20%). However, the structural-dynamic parameters are detected quite accurately, as the energy balance discussed in Section 4.3 indicates.

3.2. Method of flutter calculations

The stability of Eq. (1) is analyzed in flutter calculations. These flutter calculations are performed according to a k-method in order to calculate the flutter-stability limit from the measured aerodynamic characteristics of the airfoil. Therefore the motion of the structure is assumed to be harmonic,

$$\mathbf{u}(t) = \bar{\mathbf{u}} + \hat{\mathbf{u}}\mathrm{e}^{\mathrm{i}kt} = \begin{bmatrix} \bar{h} \\ \bar{\alpha} - \alpha_0 \end{bmatrix} + \begin{bmatrix} \hat{h}\mathrm{e}^{\mathrm{i}\phi_h} \\ \hat{\alpha}\mathrm{e}^{\mathrm{i}\phi_\alpha} \end{bmatrix} \mathrm{e}^{\mathrm{i}kt}, \tag{4}$$

with a complex $\hat{\mathbf{u}}$ and a real reduced frequency $k = \omega^* c^*/v_\infty^*$. The aerodynamic loads are also assumed to be harmonic with complex aerodynamic derivatives $c_{l/m,h/\alpha}$,

$$\begin{aligned} \mathbf{f}(t) &= \bar{\mathbf{f}} + \mathbf{A}\hat{\mathbf{u}}\mathrm{e}^{\mathrm{i}kt} \\ &= \begin{bmatrix} \bar{c}_l \\ \bar{c}_m + x_0\bar{c}_l \end{bmatrix} + \begin{bmatrix} c_{l,h} & c_{l,\alpha} + x_0 c_{l,h} \\ c_{m,h} + x_0 c_{l,h} & c_{m,\alpha} + x_0 c_{l,\alpha} \\ & +x_0(c_{m,h} + x_0 c_{l,h}) \end{bmatrix} \begin{bmatrix} \hat{h}\mathrm{e}^{\mathrm{i}\phi_h} \\ \hat{\alpha}\mathrm{e}^{\mathrm{i}\phi_\alpha} \end{bmatrix} \mathrm{e}^{\mathrm{i}kt}. \end{aligned} \tag{5}$$

For simplicity of analysis, the small damping of the system is approximated by structural damping that can be seen as an imaginary spring stiffness instead of the viscous damping,

$$2v_\infty \mathbf{D}\frac{\partial \mathbf{u}(t)}{\partial t} \approx \mathrm{i}2\begin{bmatrix} \omega_h/\omega_\alpha & 0 \\ 0 & 1 \end{bmatrix}\mathbf{D}(\mathbf{u}(t) - \bar{\mathbf{u}}). \tag{6}$$

Introducing Eqs. (4)–(6) into Eq. (1) yields

$$\left\{-v_\infty^2 k^2 \mathbf{M} + \left(\mathbf{K} + \mathrm{i}2\begin{bmatrix} \omega_h/\omega_\alpha & 0 \\ 0 & 1 \end{bmatrix}\mathbf{D}\right) - \frac{2}{\pi}\frac{v_\infty^2}{\mu}\mathbf{A}\right\}\hat{\mathbf{u}}\mathrm{e}^{\mathrm{i}kt} + \left(\mathbf{K}\bar{\mathbf{u}} - \frac{2}{\pi}\frac{v_\infty^2}{\mu}\bar{\mathbf{f}}\right) = 0. \tag{7}$$

The first term in parentheses constitutes an eigenvalue problem with $\lambda = 1/(v_\infty k)^2$,

$$\left(\mathbf{K} + \mathrm{i}2\begin{bmatrix} \omega_h/\omega_\alpha & 0 \\ 0 & 1 \end{bmatrix}\mathbf{D}\right)^{-1}\left(\mathbf{M} + \frac{2}{\pi\mu k^2}\mathbf{A}\right)\hat{\mathbf{u}} = \lambda\hat{\mathbf{u}}, \tag{8}$$

while the last term in parentheses in Eq. (7) represents the static aeroelastic equation. Since k is real and positive, the real eigenvalues λ describe the flutter-stability limit.

The structural-dynamic parameters are fixed in the experiments as given in Eqs. (2). The aerodynamic derivatives $\mathbf{A} = \mathbf{A}(k, \mathrm{Ma}_\infty, \mathrm{Re}_\infty)$ are functions of the reduced frequency, Mach number and the Reynolds number. They were measured in forced harmonic oscillation experiments at different frequencies and Mach numbers while the Reynolds number has been kept approximately constant at $\mathrm{Re}_\infty \approx 2 \times 10^6$. In order to determine the flutter-stability limit, μ and k are varied systematically to find real positive eigenvalues λ that satisfy Eq. (8). One has to keep in mind that a variation of μ at constant Mach and Reynolds numbers for a given gas and fixed structural-dynamic parameters is associated with a variation of v_∞ since μ depends on ρ_∞^*.

In the results a measured flutter boundary and the flutter-stability limit analyzed on base of measured aerodynamic derivatives are compared with the stability limit of an analytical reference case: the stability limit for an infinitesimally thin flat plate in inviscid subsonic compressible flow is predicted assuming the same structural-dynamic parameters as presented in Eq. (2). The aerodynamic derivatives for the flat plate can be determined by assuming that the unsteady flow due to harmonic oscillation can be described by the Possio (1938) integral equation. The method of Carstens (1973) is used to solve this equation numerically and to obtain the required derivatives.

4. Results and discussion

Experimental data were obtained from two kinds of experiments. In the first kind, time series were measured while the airfoil exhibits self-sustained oscillations in the flutter-test set-up. LCO test cases for checking and improving flutter prediction tools are taken from these data. Furthermore, the energy exchange between the fluid and the structure can be calculated from these data. The examination of this energy balance links the global aerodynamic force behavior to the observed LCOs. Moreover, the flutter tests yield flutter boundaries. These flutter boundaries are compared with the results of a stability analysis of the governing Eq. (1). This comparison suggests, which global aerodynamic force behavior may be responsible for the transonic dip. For the stability analysis the aerodynamic response to the pitch as well as the heave motion of the airfoil is needed. Thus, this has been measured in the second kind of experiments, forced harmonic oscillation experiments. In the following these results are presented first. Afterward, the LCO test cases are proposed before the energy exchange between the fluid and the structure is discussed.

4.1. Transonic dip

Fig. 2 shows the measured flutter and buffeting boundary in the flutter index fi/Mach number Ma_∞ plane revealing the slope of a transonic dip. The squares mark conditions where the Mach number Ma_∞ has been varied at a constant stagnation pressure until oscillations of the airfoil are neither amplified nor damped. The flutter-control system is used in the procedure to find such a condition (Schewe et al., 2003). The circles mark conditions that are extrapolated from detected values of the pitch and heave eigenfrequencies at several Mach numbers Ma_∞ for different stagnation pressure values according to Zimmermann and Weissenburger's (1964) criterion. The mean angle of attack $\bar{\alpha}$ decreases slightly with Mach number since $\bar{c}_m$ which remains nearly constant is always <0; its off-wind value α_0 is fixed and the dynamic pressure $\rho^*_\infty {v^*_\infty}^2/2$ increases with Mach number at a constant stagnation pressure. Although α_0 has been adapted to each stagnation pressure, the angle of attack of the measured flutter boundary varies about $\pm 0.13^\circ$. Furthermore, the variation of Mach number Ma_∞ and stagnation pressure corresponds to a variation of the Reynolds number $\mathrm{Re}_\infty/10^6 \approx 2.09 \pm 0.75$ since the chord length of the airfoil is fixed and the stagnation temperature and thus the Sutherland constant $\mathrm{Su}_0 = 110.4\mathrm{K}/T^*_0$ remains almost constant. At $\mathrm{Ma}_\infty = 0.789$, buffeting is assumed to occur since the observed oscillations changed from combined pitch/heave oscillations with a pronounced peak in the power spectrum of the motion data at a typical reduced frequency $k \approx 0.3$ to pitch dominated oscillations of the structure at about $k = 0.482$ showing a broader peak in the power spectrum. This frequency does not match any structural eigenfrequency and is thus determined by the flow. So, self-excited shock-induced oscillations seem to occur which interact with the structure as buffeting.

In Fig. 2 the measured flutter boundary is compared with the flutter-stability limit analyzed based on the aerodynamic derivatives of an infinitesimal thin flat plate in inviscid subsonic compressible flow (Section 3.2). The corresponding stationary pressure distributions at several Mach numbers in Fig. 2 reveal that discrepancies between the stability boundary of the flat plate and the NLR 7301 correspond to the appearance of shock waves in the flowfield. The measured flutter boundary is also compared with flutter-stability limits analyzed from derivatives measured by the balance and by the pressure transducers described in Section 2. The slope of both curves with the two local minima matches qualitatively well to the measured one. But the quantitative agreement between the pressure-based data and the measured boundary is moderate. This is probably caused by a small torsion of the model. Although its carbon-fiber composite structure is very stiff and the model is mounted at both sides, the midsection rotates against the roots. Static deformation tests have shown that this torsion may amount up to 0.05° at common loads. The pitching amplitudes of the midsection may differ from those of the roots by up to 4%, with a phase lag smaller than 1.5° at typical flutter frequencies as accelerometer responses in forced pitch oscillation experiments revealed. This small torsion of the model may influence the pressure-based derivatives measured in the midsection. Thus, the agreement between the balance-based stability limits considering the global forces and the measured flutter boundary is much better.

In order to clarify which global force behavior is responsible for the observed transonic dip, the sensitivity of the stability limit to the four complex derivatives is surveyed. Fig. 3 shows on the left side the magnitude and phase distributions of balance-based data measured from the NLR 7301 and theoretically obtained derivatives for the flat plate versus Mach number for forced harmonic pitch and heave oscillations at reduced frequencies corresponding to the stability limit of Fig. 2. On the right side of Fig. 3, the measured flutter and buffeting boundary is compared with flutter-stability limits analyzed from the measured balance derivatives combined with the theoretically obtained derivatives. For the combinations, in general, the theoretical values are applied, except for either one measured magnitude or one measured phase distribution. Replacing the magnitude distributions did not reveal slopes that differ essentially from the flat plate stability limit. Only the stability limit where the measured phase distribution of the $c_{l,\alpha}$ is applied (gray shaded combination in Fig. 3) matches the measured curve qualitatively. This suggests that the time lag of the lift response to

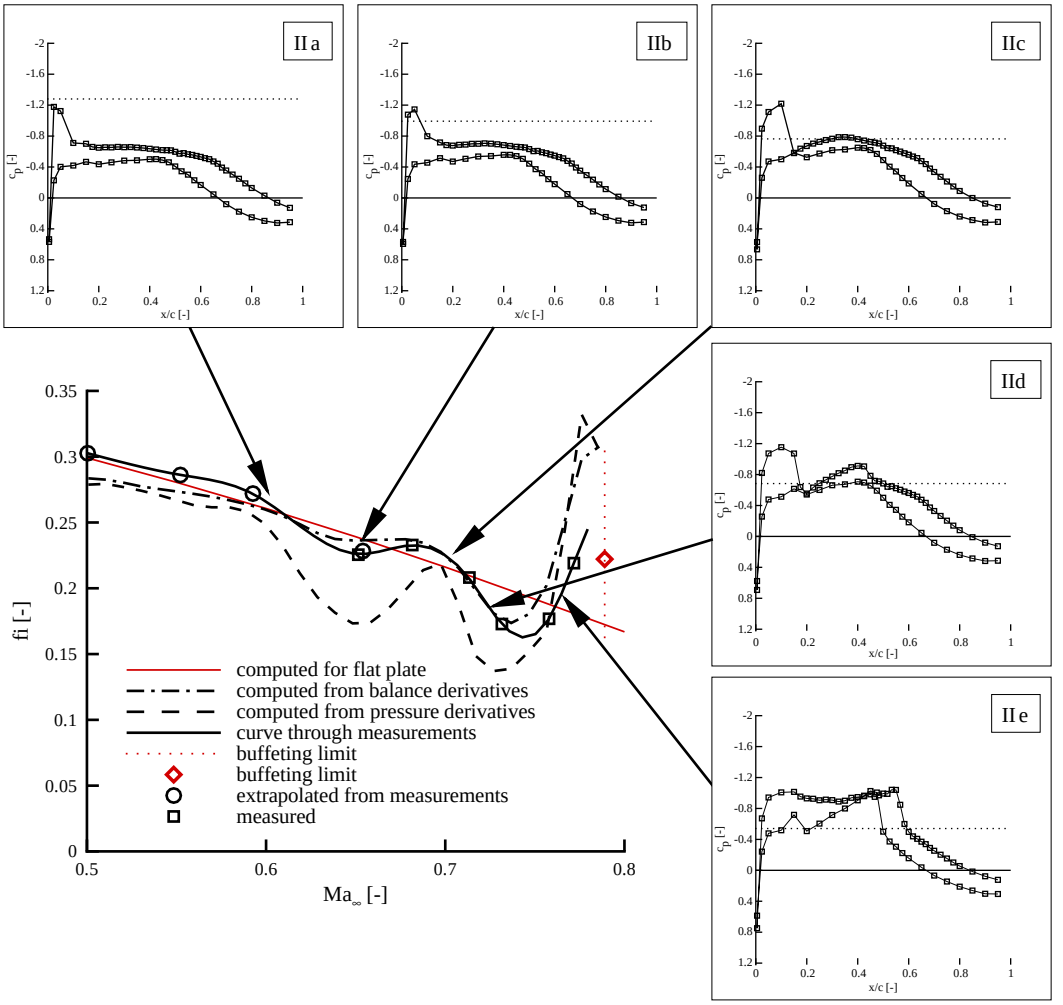

Fig. 2. Comparison of a measured/extrapolated (Zimmermann and Weissenburger, 1964) flutter and buffeting boundary at $\alpha = 0.46^\circ \pm 0.13^\circ$, $Su_0 = 110.4K/T_0^* = 0.365 \pm 1.5\%$ with flutter-stability limits analyzed from derivatives measured by a balance and by pressure transducers at $\alpha = 0.33 \pm 0.05^\circ$, $Re_\infty = 2.21 \times 10^6 \pm 9.3\%$ as well as to a flutter-stability limit analyzed from theoretically obtained derivatives for a flat plate. Corresponding measured stationary pressure distributions with lines marking $c_{p\ \mathrm{crit}}$.

the pitch motion of the airfoil may be responsible for the characteristic shape of the transonic dip. This proposition will be discussed further in Section 4.3. Next, the behavior of the fluid–structure system in the unstable region close to the transonic dip will be discussed.

4.2. Limit-cycle-oscillation test cases

In the present study various types of LCOs with small amplitudes, even multiple nested ones, have been observed in the unstable region close to the transonic dip. In principle, the experiments in the adaptive test-section of the TWG revealed similar manifestations of LCOs as described by Schewe et al. (2003). In addition to the transition tripping at 7%/14% chord on the suction/pressure side, the adaptive walls provide a well-defined solid-wall boundary condition for numerical simulations. Furthermore, steady wall adaptation is necessary although not sufficient in order to obtain interference-free unsteady results (Voß, 1998), but the residual wind-tunnel wall interference is minimized so that a comparison with free-flight simulations could be reasonable. This suggests that additional LCO test cases should be defined as complement to the Schewe et al. (2003) MP77 obtained in the perforated test-section of the TWG.

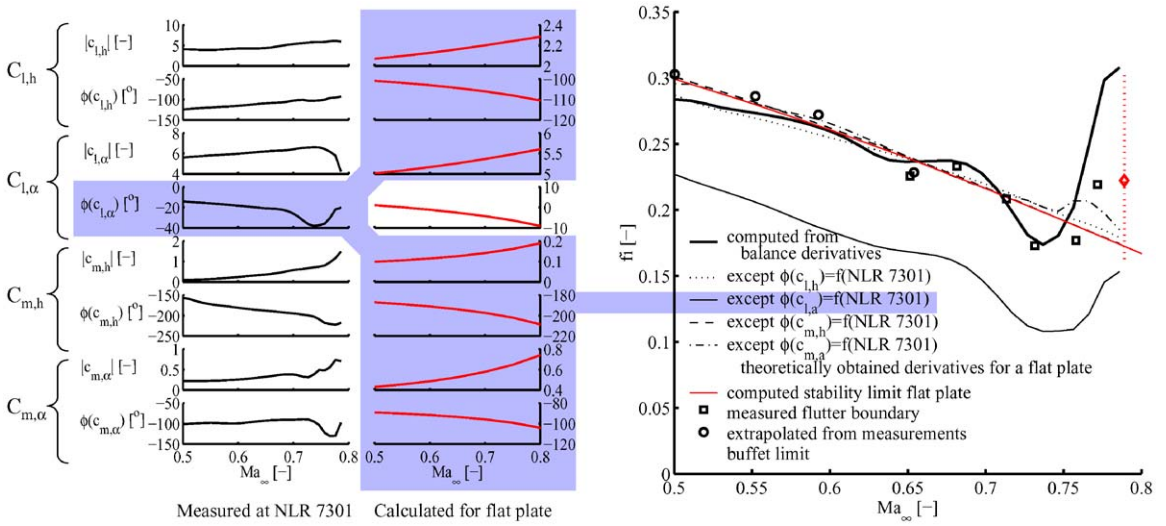

Fig. 3. Left: Magnitude and phase distributions of measured and theoretically obtained derivatives versus Mach number for forced harmonic pitch and heave oscillations at reduced frequencies corresponding to the stability limit of Fig. 2; Right: Comparison of a measured flutter and buffeting boundary at $\alpha = 0.46 \pm 0.13^\circ$, $\mathrm{Su}_0 = 110.4\mathrm{K}/T_0^* = 0.365 \pm 1.5\%$ with flutter-stability limits analyzed from measured balance derivatives at $\alpha = 0.33 \pm 0.05^\circ$, $\mathrm{Re}_\infty = 2.21 \times 10^6 \pm 9.3\%$ combined with theoretically obtained derivatives for a flat plate.

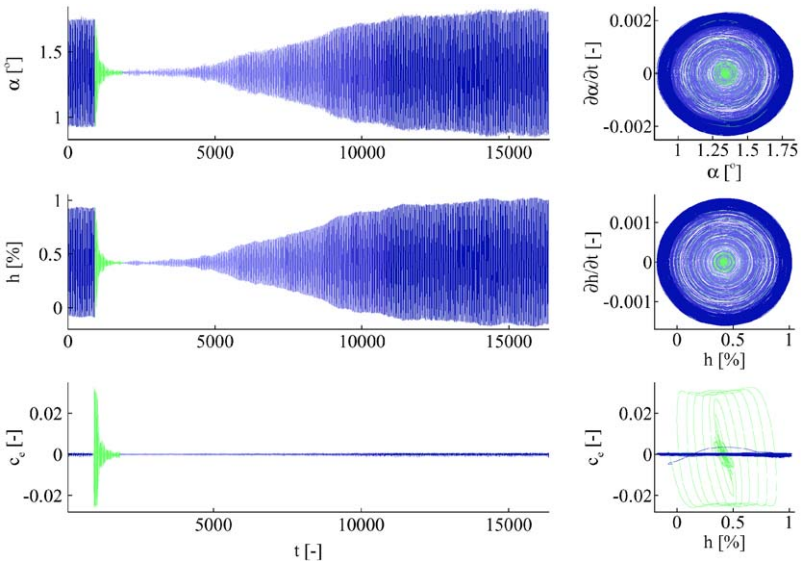

Fig. 4. Left: Time series of the pitch α and the heave h motion as well as the exciter-force coefficient $c_e(t) = F_e^*(t)/\left(\frac{1}{2}\rho_\infty^* v^{*2} c^* b^*\right)$ for test case TL2. Right: Corresponding phase-space representation.

Fig. 4 shows on the left the time history of the pitch $\alpha(t)$ and the heave $h(t)$ motion of the proposed test case TL2. At the beginning of the time series, the airfoil exhibits combined pitch and heave motions. By use of the flutter-control system these oscillations are damped out between $900 < t < 1800$. The forces applied by the electrodynamic exciters in heave direction c_e are shown in the lower part of Fig. 4 and are nondimensionalized in the same manner as the lift coefficient. The maximum amplitude of the forces that are applied to control the LCO $\hat{c}_e \approx 0.03$ are remarkably small compared with typical lift coefficients. At $t \approx 1800$ the flutter-control system is switched off into open-loop state and the amplitudes of the oscillations grow to the LCO state without any artificial excitation. On the right of Fig. 4, the corresponding phase-space representation of the observed oscillations are shown. Due to the appropriate scaling, the

Table 1
Limit-cycle oscillation test cases TL1 and TL2

Flow and structural parameters			Measured LCO properties		
	TL1	TL2		TL1	TL2
l..l.. Ma_∞	0.745	0.691	$\bar{\alpha}$	-0.01°	1.34°
$Re_\infty/10^6$	2.27	1.46	$\bar{c}_l$	0.193	0.380
Su_0	0.362	0.365	$\bar{c}_m$	−0.051	−0.053
μ	705.3	1013.2	$\hat{h}$	0.20%	0.57%
v_∞	2.84	2.65	$\hat{\alpha}$	0.20°	0.46°
α_0	$0.68^\circ \pm 0.04^\circ$	$1.78^\circ \pm 0.04^\circ$	$\hat{h}/\hat{\alpha}$	0.58	0.71
			$\phi_\alpha - \phi_h$	171°	178°
			k	0.257	0.269
			n	≈110	≈390

trajectories in the LCO state are shaped approximately circular. This indicates that the pitch and heave motion of the airfoil behave almost harmonically. A flutter-divergence interaction (Bendiksen, 1992) could be observed for neither TL1 nor TL2, since the mean angle of attack for the LCOs is the same as the one for the damped state.

The flow and structural parameters of the proposed test cases TL1 and TL2 are reported in Table 1. The measured LCO properties like amplitudes of motion $\hat{h}$, $\hat{\alpha}$ as well as the reduced LCO frequency k and the approximate number of oscillation cycles n to develop into the stable LCO are also stated. Furthermore, the mean angle of attack $\bar{\alpha}$ resulting from the twist of the torsional springs due to the time-averaged pitching moment $\bar{c}_m$ as well as the time-averaged lift $\bar{c}_l$ are given in Table 1. In both cases a phase difference $\phi_\alpha - \phi_h$ of nearly 180° is observed between the heave and the pitch motion. Thus, these LCOs can be considered as a single-degree-of-freedom (sdof) motion. The amplitude ratio $\hat{h}/\hat{\alpha}$ at $\phi_\alpha - \phi_h = 180^\circ$ can be interpreted as the distance per chord between a center of rotation upstream of the airfoil and the elastic axis. Around this center the chord of the airfoil rotates approximately while performing the identified LCOs. This supports Bendiksen's (1992) observation that in transonic flow the phase difference between heave and pitch motion tends to adjust such that sdof flutter occurs.

The wind-tunnel wall shapes for the LCO test cases TL1 and TL2 are reported in Table 2. The nondimensional coordinate $z(x)$ perpendicular to the wind-tunnel axis represents the position of the jacks deflecting the flexible top and bottom walls of the adaptive test-section. The influence of the sidewall boundary layer can neither be controlled nor eliminated (Wedemeyer et al., 1998). However, its displacement effect is considered in the wall-adaptation procedure, as the displacement thickness is roughly estimated to be the same as that of a turbulent boundary layer with a zero pressure gradient for both sidewalls. The result is added to the desired wall shapes (Jacobs, 2002). Therefore this displacement thickness is subtracted from z to obtain the coordinate z_{2D}. Thus, z_{2D} should be used for simulations assuming viscid 2-D flow between solid top and bottom wind-tunnel walls.

Measured steady state pressure distributions at flow parameters close to those of TL1 and TL2 are presented in Fig. 5. They are shown with pressure and skin-friction distributions that are obtained by integrating the coupled Euler- and boundary-layer equations by using the code MSES of Drela and Giles (1987), assuming free-flight farfield boundary conditions. For both simulated cases, Mach Ma_∞ and Reynolds number Re_∞ as well as angle of attack α are taken as measured without any corrections. In the right, the measured and simulated pressure distribution match fairly well, while in the left, a discrepancy between the measured and computed strength of the shocks can be observed. However, the pressure recovery at the trailing edge is predicted quite well in both cases. This agreement of the pressure distributions indicates the effectiveness of the wind-tunnel wall adaptation. Furthermore, the simulations show in the skin-friction distributions that the boundary layer tends to separate near the trailing edge of the suction side for TL1 and TL2. It is assumed to be essential to match the main characteristics of the flowfield, such as shock position or separation topology in numerical simulations in order to get a reasonable agreement with the measured LCO behavior (Schewe et al., 2003).

Fig. 6 shows several LCO property trends dependent on the Mach number Ma_∞ in the vicinity of the proposed test cases TL1 and TL2. These trends may help to adjust parameters of a numerical simulation and to compare the computed LCO behavior at flow conditions close to those of the two test cases. The Mach number is varied, while the stagnation pressure and the stagnation temperature of the wind tunnel flow is kept constant. Thus, the dimensional freestream velocity v^*_∞ increases and the dimensional freestream density ρ^*_∞ decreases with increasing Mach number. This yields the increasing reduced velocity v_∞ and the slightly increasing mass ratio μ that can be seen in Fig. 6(d). The mean angle of attack $\bar{\alpha}$ decreases with increasing Mach number since $\bar{c}_m \approx -0.05$ and is nearly constant and the v^2_∞/μ

Table 2
Wind-tunnel wall shapes[a] for LCO test cases TL1 and TL2

Upper wall (suction side)					Lower wall (pressure side)				
	TL1		TL2			TL1		TL2	
−8.2167	1.6667	1.6667	1.6667	1.6667	−8.2167	−1.6667	−1.6667	−1.6667	−1.6667
−6.9833	1.6667	1.6637	1.6667	1.6635	−6.9833	−1.6667	−1.6637	−1.6667	−1.6635
−5.8833	1.6707	1.6658	1.6729	1.6676	−5.8833	−1.6655	−1.6606	−1.6633	−1.6580
−5.0833	1.6747	1.6685	1.6786	1.6719	−4.9500	−1.6664	−1.6600	−1.6622	−1.6552
−4.2833	1.6794	1.6720	1.6854	1.6773	−4.0500	−1.6670	−1.6593	−1.6606	−1.6521
−3.4833	1.6848	1.6762	1.6928	1.6835	−3.1500	−1.6676	−1.6585	−1.6586	−1.6487
−2.6833	1.6908	1.6811	1.7014	1.6908	−2.3167	−1.6687	−1.6585	−1.6569	−1.6457
−1.9167	1.6984	1.6876	1.7118	1.7000	−1.4833	−1.6713	−1.6599	−1.6561	−1.6437
−1.1500	1.7084	1.6966	1.7243	1.7113	−0.7833	−1.6755	−1.6632	−1.6570	−1.6436
−0.5500	1.7190	1.7063	1.7360	1.7222	−0.2167	−1.6804	−1.6674	−1.6593	−1.6451
−0.0833	1.7276	1.7144	1.7446	1.7301	0.2500	−1.6835	−1.6698	−1.6616	−1.6466
0.2500	1.7318	1.7182	1.7484	1.7335	0.7167	−1.6842	−1.6699	−1.6632	−1.6476
0.5833	1.7328	1.7187	1.7489	1.7335	1.2500	−1.6834	−1.6684	−1.6649	−1.6485
1.0500	1.7305	1.7158	1.7458	1.7298	1.8833	−1.6832	−1.6675	−1.6678	−1.6506
1.5833	1.7260	1.7106	1.7402	1.7234	2.5167	−1.6843	−1.6678	−1.6719	−1.6538
2.1833	1.7218	1.7057	1.7341	1.7165	3.1500	−1.6861	−1.6688	−1.6761	−1.6572
2.7833	1.7185	1.7016	1.7288	1.7104	3.6833	−1.6877	−1.6697	−1.6797	−1.6601
3.2833	1.7165	1.6990	1.7252	1.7061	4.2167	−1.6896	−1.6710	−1.6833	−1.6629
3.7167	1.7153	1.6973	1.7225	1.7028	4.7500	−1.6915	−1.6723	−1.6867	−1.6657
4.1500	1.7139	1.6954	1.7198	1.6996	5.3833	−1.6936	−1.6736	−1.6904	−1.6686
4.6500	1.7124	1.6933	1.7170	1.6962	6.0500	−1.6955	−1.6747	−1.6940	−1.6713
5.2500	1.7115	1.6917	1.7146	1.6929	6.7167	−1.6961	−1.6745	−1.6958	−1.6722
5.9833	1.7124	1.6917	1.7135	1.6909	x	z	z_{2d}	z	z_{2d}
6.7167	1.7115	1.6899	1.7110	1.6874					
x	z	z_{2d}	z	z_{2d}					

[a] Origin of the coordinate system in the leading edge at $x = 0, z = 0$ of the airfoil without loads at $\alpha = 0°$, the coordinates are made nondimensional by the chord length c^* of the airfoil.

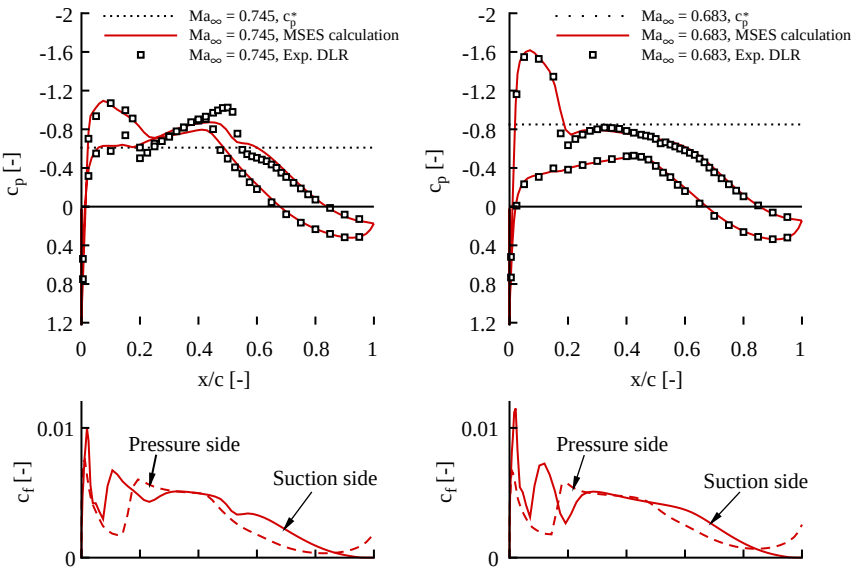

Fig. 5. Measured steady state pressure distributions at flow parameters close to those of TL1 and TL2 compared with pressure and skin-friction distributions simulated with the Drela and Giles (1987) Euler/boundary-layer code MSES. Left: $Ma_\infty = 0.745$, $Re_\infty = 2.26 \times 10^6$, $Su_0 = 0.361$, $\alpha = 0.02°$. Right: $Ma_\infty = 0.683$, $Re_\infty = 2.16 \times 10^6$, $Su_0 = 0.362$, $\alpha = 1.31°$.

increases with Mach number (Fig. 6(c), last term in Eq. (7)). Fig. 6(a) should not be interpreted as a bifurcation diagram in order to distinguish between a sub- and a supercritical bifurcation (Schewe et al., 2003) since the Mach number resolution is poor and at least two stability parameters Ma_∞ and $\bar{\alpha}$ are changed simultaneously. But, the oscillation-amplitude trends presented in Fig. 6(a) indicate that the LCO behavior of the proposed test cases is more or less "benign". This can also be seen by examining the approximate number of oscillation cycles $n \approx \mathcal{O}(100)$ (Table 1) to develop into the stable LCO state. In both cases, Fig. 6(a) shows finite amplitudes of motion even at stable flow conditions. Although the turbulence level of the wind tunnel is small with 0.1% at $\mathrm{Ma}_\infty = 0.5$ up to 0.25% at $\mathrm{Ma}_\infty = 0.8$ (Jacobs, 2002), these small disturbances provoke small oscillations of the airfoil. These disturbances also initiate the growing amplitudes in unstable regions as shown in Fig. 4. Fig. 6(b) shows only slightly varying frequency ratios k/k_α while the amplitude ratio $\hat{h}/\hat{\alpha}$ increases with increasing Mach number. Since the phase difference $\phi_\alpha - \phi_h$ is approximately 180°, the center of rotation of the chord of the airfoil moves upstream with increasing Mach number. However, compared with the results of Schewe and Deyhle (1996) and Schewe et al. (2002, 2003), the reported LCO amplitudes are considerably smaller than those shown in the numerical results which are mentioned in the introduction. Nevertheless, there might be other coexisting or nested LCO attractors of higher amplitude around the presented ones that were not found. At least one additional "stall" attractor and one repeller between both the attractors should exist theoretically. However, at other flow conditions coexisting nested LCOs were observed with a similar behavior as described by Schewe et al. (2003). So-called subcritical bifurcations (Schewe et al. 2003) were also observed. In this case a repeller exists between the stable fixpoint and the first stable LCO attractor and a traditional flutter-stability analysis would predict safe flight conditions although a gust could initiate limit-cycle oscillations.

4.3. Energy exchange in limit-cycle oscillations

The law of conservation of energy states that the sum of the kinetic energy in the heave and the pitch motion E_{kin} together with the potential energy in the springs E_{pot} must be equal to the constant initial energy $E_0 = E_0^*/(\rho_\infty^*/2 v_\infty^{*2} c^{*2} b^*)$ in the structural-dynamic system plus the sum of work of the nonconservative forces ΣW, while energy is dissipated due to the structural damping. The power dissipated by the structural damping is $P_v = P_v^*/(\rho_\infty^*/2 v_\infty^{*3} c^* b^*)$. The lift and the pitching moment perform the energy exchange between flow and structure at $P_l + P_m$ per unit time. Beside this the flutter-control system puts the power ($P_e > 0$) in or takes the power ($P_e < 0$) out of the structural-dynamic system. So,

$$E_0 = E_{\mathrm{kin}} + E_{\mathrm{pot}} - W = E_{\mathrm{kin}} + E_{\mathrm{pot}} - \int (P_v + P_l + P_m + P_e)\,\mathrm{d}t \tag{9}$$

represents an integral of the equation of motion (1) and thus describes the energy balance for the two-degree-of-freedom system around its steady position $\bar{u}$ with

$$E_{\mathrm{kin}} = \frac{\pi\mu}{4}\frac{\partial u^{\mathrm{T}}}{\partial t}\mathbf{M}\frac{\partial u}{\partial t}, \quad E_{\mathrm{pot}} = \frac{\pi\mu}{4v_\infty^2}(u-\bar{u})^{\mathrm{T}}\mathbf{K}(u-\bar{u}), \quad P_v = -\frac{\pi\mu}{v_\infty}\frac{\partial u^{\mathrm{T}}}{\partial t}\mathbf{D}\frac{\partial u}{\partial t},$$

$$P_m = (c_m - \bar{c}_m)\frac{\partial \alpha}{\partial t}, \quad P_l = (c_l - \bar{c}_l)\left(\frac{\partial h}{\partial t} + x_0\frac{\partial \alpha}{\partial t}\right), \quad P_e = c_e\frac{\partial h}{\partial t}. \tag{10}$$

Fig. 7 shows the time history of the total energy $E = E_{\mathrm{kin}} + E_{\mathrm{pot}}$ compared with the work of the nonconservative forces for a measured time series where the system exhibits an LCO that is damped at time $t = 1800$ until $t = 4800$ and is excited at time $t = 8500$. The total energy and the work agree satisfactorily. That indicates that the structural-dynamic parameters of Eqs. (2) and the time series of the motion and the forces were measured with sufficient accuracy, since many possible inaccuracies, e.g., improper damping coefficients, would lead to an accumulating discrepancy of the integral with respect to time of the power terms compared with the sum of energy (cf. Fig. 7, with Lehr's plunge-damping coefficient assumed to be 110% δ_h). The time traces and the amplitude dependency of the different power terms of this energy balance give some enlightenment as to which aerodynamic force behavior is responsible for the amplitude limitation of the observed LCOs. Therefore the LCO amplitude at a given set of flow and structural parameters is varied by using the flutter-control system in order to extract energy out of or to add energy to the oscillating system.

Fig. 8 demonstrates the results of this method: on the left side several components of power averaged per oscillation cycle are plotted against the limit-cycle pitch amplitude squared. The LCO amplitude has been adjusted by the flutter-control system in the following way: at conditions near the transonic dip where the airfoil exhibits limit-cycle oscillations, the LCO has been damped out artificially. Then, the damping factor of the flutter-control system was reduced gradually. For different damping factors the LCO amplitudes were recorded and the energy exchange between

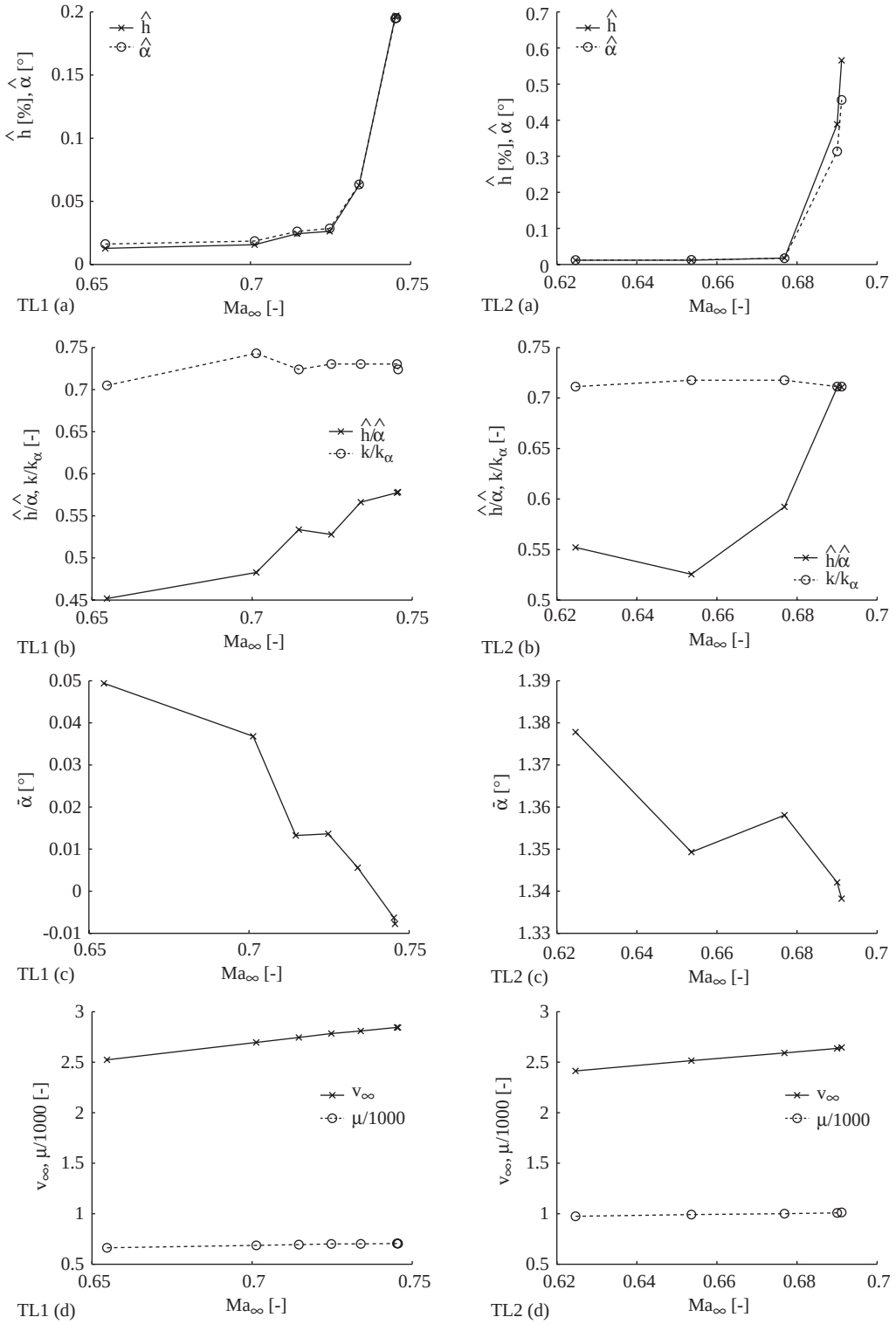

Fig. 6. Mach-number-dependent behavior of LCO relevant properties in the vicinity of the proposed test cases TL1 and TL2: (a) $\hat{h}$ heave and $\hat{\alpha}$ pitch amplitude, (b) $\hat{h}/\hat{\alpha}$ heave/pitch amplitude ratio and reduced flutter frequency k as well as (c) $\bar{\alpha}$ mean angle of attack, (d) corresponding Mach-number-dependent changes of the parameters reduced speed v_∞ and mass ratio μ.

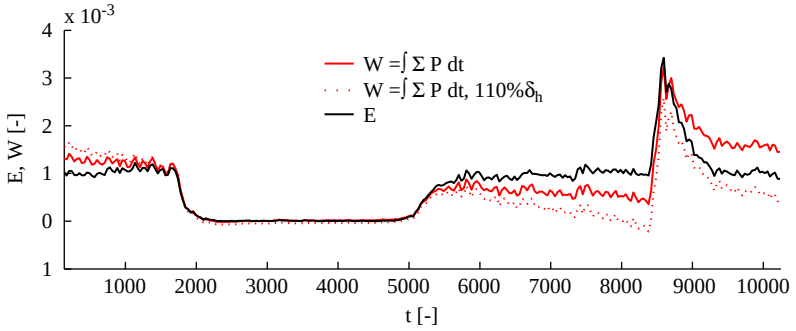

Fig. 7. Comparison of the total energy $E = E_{\text{kin}} + E_{\text{pot}}$ and the work applied by nonconservative forces $W = \int \Sigma P \, dt$ calculated according to Eq. (10) from a measured time series and the structural-dynamic parameters of Eq. (2). The flutter-control system is used at time 1800 to damp an LCO until time 4800 and at time 8500 to excite the system.

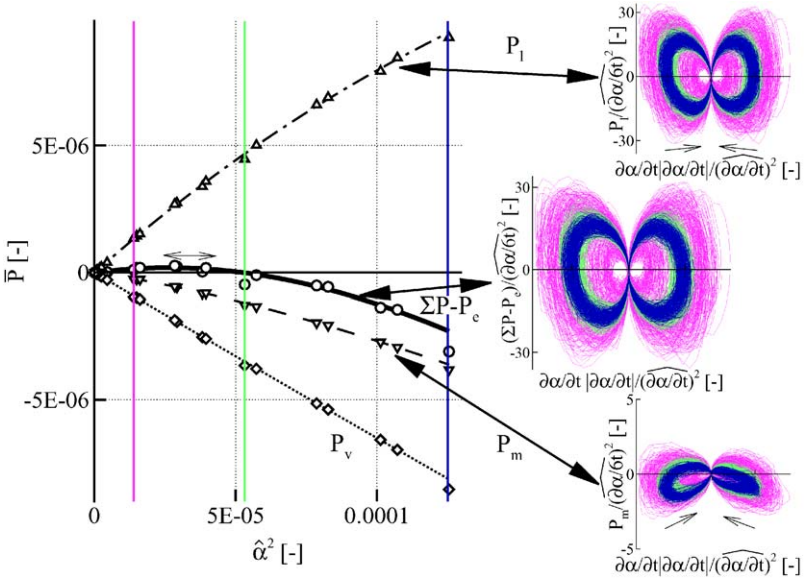

Fig. 8. Left: Components of power $\bar{P}_l, \bar{P}_m, \bar{P}_v, \Sigma\bar{P} - \bar{P}_e$ averaged per oscillation cycle versus limit-cycle pitch amplitude squared $\hat{\alpha}^2$. Right: Instantaneous components of power $P_l, P_m, \Sigma P - P_e$ versus pitching velocity times its absolute value $\partial\alpha/\partial t|\partial\alpha/\partial t|$. Ordinate and abscissa are normalized by the amplitude of the pitching velocity squared $\partial\hat{\alpha}/\partial t^2$. $\text{Ma}_\infty = 0.691 \pm 0.05\%$, $\text{Re}_\infty = 1.47 \times 10^6 \pm 0.8\%$, $\text{Su}_0 = 0.367 \pm 0.6\%$, $\mu = 1008.9 \pm 0.6\%$, $v_\infty = 2.64 \pm 0.3\%$, $\alpha_0 = 1.78^\circ \pm 0.04^\circ$.

the fluid and the structure was observed. When the damping factor has been reduced to zero, the curve $\Sigma\bar{P} - \bar{P}_e$ crosses the zero axis at the naturally occurring LCO amplitude, since no power is exchanged with the flutter-control system. Then the flutter-control system has been switched to excitation and the amplification factor was increased gradually until the LCO exhibited an amplitude greater than twice the unexcited one. Later the flutter-control system was gradually increased to damp the oscillations again in order to demonstrate that no hysteresis occurs. It is remarkable that for all LCO amplitudes larger than 10% of its maximum value the LCO properties $\hat{h}/\hat{\alpha} = 0.709 \pm 1.4\%$, $\phi_\alpha - \phi_h = 178.2^\circ \pm 0.7^\circ$ and $k = 0.270 \pm 0.8\%$ remain almost constant although the flutter-control system introduces forces in heave direction. Fig. 8 demonstrates on the left that both the power $\bar{P}_v$ due to the structural damping and the power $\bar{P}_m$ due to the pitching moment withdraw energy from the oscillating system, because both components are negative (cf. sign convention in Eqs. (9) and (10)). Since the abscissa is the limit-cycle pitch amplitude squared $\hat{\alpha}^2$, $\bar{P}_v$ appears as a straight line. In the case of "classical" flutter exhibiting exponentially growing oscillation amplitudes, the sum of power $\Sigma\bar{P} - \bar{P}_e$ would be a straight line in such a diagram, too. But, since the curves of $\bar{P}_m$ and $\bar{P}_l$ are slightly nonlinear, the

sum of power $\Sigma\bar{P} - \bar{P}_e$ is also nonlinear and is able to cut the abscissa at a distinct amplitude $\hat{\alpha}^2$. This argument, while having in mind that the motion of the airfoil is almost harmonic, leads to the following proposition: the amplitude dependency of the imaginary part of the lift or of the pitching-moment response to the motion of the airfoil is necessary for the amplitude limitation of the observed LCOs. A slight variation of the structural damping would change the LCO amplitude significantly, since the curve $\Sigma\bar{P} - \bar{P}_e$ crosses the abscissa at a fine angle and would then rotate around the origin. Thus, the LCO amplitude strongly depends on the structural damping in the system. This statement is in agreement with Meijer and Cunningham (1992) who found that the damping is important for the correctly modelling LCO amplitude. It also supports Morton and Beran's (1999) speculation, that differences in the numerical dissipation and the applied time steps cause discrepancies in the LCO amplitude prediction. A stable LCO attractor requires that $\Sigma\bar{P} - \bar{P}_e$ decreases with increasing oscillation amplitude while cutting the abscissa. Conversely, if a repeller is present, the sum of power would have to increase with the oscillation amplitude close to $\Sigma\bar{P} - \bar{P}_e = 0$.

The diagram on the left side of Fig. 8 reveals that the power due to the lift feeds energy into the oscillations. This fortifies the presumption of Section 4.1: in the vicinity of the transonic dip, the time lag of the lift response to the motion of the airfoil yields a power flux into the oscillating system. The significance of the lift supports the argumentation of Bendiksen (1992). He claims that the tendency to transonic sdof flutter may be caused by a maximum work contribution of the lift variation due to the moving shock wave. Bendiksen (1992) argues on the basis of a shock-doublet approximation of Ashley (1980) that this work contribution is maximum if the shock motion is in phase with the heave velocity at the shock location and if the heave velocity at this location is maximized. The phase differences between heave and pitch motion observed in the present investigation agree with his argument. Moreover, the phase lag of the lift response to the pitching of the airfoil demonstrates a tendency to grow toward -90° in the vicinity of the transonic dip (cf. Fig. 3), such that the lift response tends to get in phase with the heave velocity. If this is caused by the shock motion being in phase with the local heave velocity, this cannot be determined since neither local forces nor flowfield information were measured in the present flutter experiments. The local aerodynamics and the local energy exchange between the fluid and structure will be the subject of future investigations.

The right side of Fig. 8 shows several instantaneous components of power versus pitching velocity times its absolute value ($\partial\alpha/\partial t|\partial\alpha/\partial t|$). The orientation of these trajectories is indicated by the arrows. The abscissa is chosen thus, in order to distinguish between the up- and downstroke of the airfoil. The trajectories are plotted for three different LCO amplitudes corresponding to the vertical gray lines in the left diagram. Abscissa and ordinate are normalized by the amplitude of the pitching velocity squared in order expose discrepancies in shapes. However, it is very difficult to recognize that the power due to the lift and the moment, averaged per cycle, decreases as shown in the left side of Fig. 8. Moreover, there is no part of the oscillation cycle that one can identify in which an eminent power loss takes place. Thus, the nonlinearities leading to the amplitude limitation of the measured LCOs are clearly small. In the lower right part of Fig. 8, a viscous damper would occur as a wedge $\wedge$ with the kink in the origin. Therefore, it is shown that the pitching moment acts more or less like a damper; but, compared with the amplifying power due to the lift, the damping power due to the moment was small in all observed cases (cf. axis limits on Fig. 8, right). However, the nonlinear increase of the damping moment could clearly be observed, whereas the nonlinear decrease of the driving power to the lift could not be confirmed for any condition.

5. Concluding remarks

Results from experiments on heave/pitch flutter of the supercritical airfoil NLR 7301 with tripped laminar-turbulent transition at transonic flow conditions have been reported. The global aerodynamic force behavior was linked to the observed transonic dip phenomena and limit-cycle oscillations. Two LCO test cases obtained in an adaptive test-section were proposed for comparison with numerical simulations.

The most significant results from this investigation can be summarized as follows.

(i) The phase lag of the lift response to the airfoil pitch motion may be responsible for the reduction of the flutter stability at transonic speeds called transonic dip.
(ii) A slightly nonlinear oscillation-amplitude dependency of the lift and the pitching moment affects the amplitude limitation of the limit-cycle oscillations.
(iii) The LCO amplitude can be controlled by relatively small forces.
(iv) The amplitudes nevertheless strongly depend on the structural damping of the aeroelastic system.

Since these results are obtained using one airfoil shape with a limited range of structural-dynamic parameter variation, it is not claimed that the present results are generally transferable to the flutter behavior of large aspect-ratio

wings. In particular, the mass ratio μ in the order of $\mathcal{O}$ (1000) is high compared with realistic configurations. Thus, for real aircraft, the aerodynamics are more dominant compared with the structural dynamics than in our experiments, according to Eq. (1). Therefore, the aerodynamic amplitude-limiting effects are stronger, but also the oscillation amplitudes in real flight will increase more rapidly, since the ratio of aerodynamic work to total energy scales with $1/\mu$ (cf. Eq. (10)). Nevertheless, the results indicate the following consequences.

(a) Although or just because LCOs are controllable with small forces, its amplitude strongly depends on the system damping. Thus, LCOs are, in the authors' opinion, only marginally usable in order to extend the operational flight regime of aircraft with large aspect-ratio wings (cf. Introduction). However, LCOs are technically very important in the context of flutter since traditional flutter-stability analysis underestimates the instability of the coupled fluid–structure system in the case of a subcritical bifurcation.
(b) Since manifestations of LCOs are rather sensitive to flow and structural parameters as well as to boundary conditions, the capability of a computational aeroelasticity code to reproduce the LCO amplitude is a telling test of the code.
(c) The reduction of the flutter stability, called transonic dip, is caused by the aerodynamic response to the motion of an airfoil with finite thickness. At transonic conditions, the unsteady flowfield depends on the steady flowfield and therefore on the airfoil incidence and shape (Tijdeman and Seebass, 1980). Thus, arranging the steady flowfield appropriately may cause unsteady flow that does not lead to a pronounced dip. So, design criteria for airfoil shapes in order to minimize the transonic dip could be formulated from the aeroelastic point of view, if the aerodynamics that leads to the time lag of the lift response to the airfoil pitch motion is understood.

The present investigation links the global force behavior to the observed motions of an airfoil. For future work we intend to examine the local aerodynamics leading to the reported global force behavior. Furthermore, we intend to enlarge the range of structural-dynamic parameter variation for flutter testing and to investigate wing models in flutter experiments in order to ensure the transferability of the obtained results to the flutter behavior of real large aspect-ratio wings.

Acknowledgements

We are grateful to Dr V. Carstens for providing the code to solve the Possio integral equation and wish to thank Dr K. Weinman, Dr W. Wegner, Dr R. Voss and Dr P. Petrie-Repar for fruitful discussions and suggestions. Thanks also to J. Nuhn for thoroughly acquiring the data as well as to J. Berold and D. Möhle being responsible for the models and the test set-ups. Finally, we would like to thank the staff of the TWG for their cooperation. This work was supported by the Hermann von Helmholtz-Gemeinschaft Deutscher Forschungszentren (HGF) within a project called "Aerostabil".

References

Ashley, H., 1980. Role of shocks in the "sub-transonic" flutter phenomenon. Journal of Aircraft 17, 187–197.
Bendiksen, O.O., 1992. Role of shock dynamics in transonic flutter. AIAA Paper 92-2121.
Carstens, V., 1973. Berechnung der instationären Druckverteilung an harmonisch schwingenden Gittern in ebener Unterschallströmung. DLR IB 253-73 J06.
Castro, B.M., Ekaterinaris, J.A., Platzer, M.F., 2001. Analysis of the effect of porous wall interference on transonic airfoil flutter. AIAA Paper 2001-2725.
Cebeci, T., Bradshaw, P., 1979. Momentum Transfer in Boundary Layers. McGraw-Hill, New York.
Drela, M., Giles, M.B., 1987. Viscous-inviscid analysis of transonic and low Reynolds number airfoils. AIAA Journal 25, 1347–1355.
Edwards, J.W., 1996. Transonic shock oscillations and wing flutter calculated with an interactive boundary layer coupling method. EUROMECH-Colloquium 349, Simulation of Fluid–Structure Interaction in Aeronautics, Göttingen, Germany.
Edwards, J.W., Bennett, R.M., Whitlow, W., Seidel, D.A., 1983. Time-marching transonic flutter solutions including angle-of-attack effects. Journal of Aircraft 20, 899–906.
Edwards, J.W., Schuster, D.M., Spain, C.V., Keller, D.F., Moses, R.W., 2001. MAVRIC flutter model transonic limit cycle oscillation test. NASA TM 2001-210877.
Jacobs, M., 2002. Treatment of the wall boundary layer in the wall adaptation procedure and steady wall adaptation for dynamic tests. Private communication, DNW BU GuK, Göttingen.
Knipfer, A., Schewe, G., 1999. Investigation of an oscillating supercritical 2D wing section in transonic flow. AIAA Paper 99-0653.

Meijer, J.J., Cunningham Jr., A.M., 1992. Development of a method to predict transonic limit cycle oscillation characteristics of fighter aircrafts. AGARD CP 507.

Morton, S.A., Beran, P.S., 1999. Hopf-bifurcation analysis of airfoil flutter at transonic speeds. Journal of Aircraft 36, 421–429.

Possio, C., 1938. L'azione aerodinamica sul profilo oscillante in un fluido compressibile a velocita iposonora. L'Aerotecnica 18, 441–458.

Rivera, J.A., Dansberry, B.E., Farmer, M.G., Eckstrom, C.V., Seidel, D.A., Bennet, R.M., 1991. Experimental flutter boundaries with unsteady pressure distributions for the NACA 0012 benchmark model. AIAA Paper 91-1010-CP.

Rivera, J.A., Dansberry, B.E., Bennett, R.M., 1992. NACA 0012 benchmark model experimental flutter results with unsteady pressure distributions. AIAA Paper 92-2396-CP.

Schewe, G., 1991. Force measurements in aeroelasticity using piezoelectric multicomponent transducers. Proceedings International Forum on Aeroelasticity and Structural Dynamics, DGLR 91-06, Aachen, Germany.

Schewe, G., Deyhle, H., 1996. Experiments on transonic flutter of a two-dimensional supercritical wing with emphasis on non-linear effects. Proceedings Royal Aeronautical Society Conference on "Unsteady Aerodynamics", London, UK.

Schewe, G., Knipfer, A., Mai, H., Dietz, G., 2002. Experimental and numerical investigation of nonlinear effects in transonic flutter. DLR IB 232-2002.

Schewe, G., Mai, H., Dietz, G., 2003. Nonlinear effects in transonic flutter with emphasis on manifestations of limit cycle oscillations. Journal of Fluids and Structures 18, 3–22.

Schulze, S., 1997. Transonic aeroelastic simulation of a flexible wing section. AGARD R 822.

Tang, L., Bartels, R.E., Chen, P.C., Liu, D.D., 2003. Numerical investigation of transonic limit cycle oscillations of a two-dimensional supercritical wing. Journal of Fluids and Structures 17, 29–41.

Thomas, J.P., Dowell, E.H., Hall, K.C., 2002. Modeling viscous transonic behavior using a harmonic balance approach. AIAA Paper 2002-1414.

Tijdeman, H., 1977. Investigations of the transonic flow around oscillating airfoils. Ph.D. Thesis, Technische Hogeschool Delft, The Netherlands. Also NLR TR 77090.

Tijdeman, H., Seebass, R., 1980. Transonic flow past oscillating airfoils. Annual Review of Fluid Mechanics 12, 181–222.

Voß, R., 1998. Wall correction methods for dynamic tests. AGARD AG 336.

Weber, S., Jones, K.D., Ekaterinaris, J.A., Platzer, M.F., 2001. Transonic flutter computations for the NLR 7301 supercritical airfoil. Aerospace Science and Technology 5, 293–304.

Wedemeyer, E., Taylor, N.J., Holst, H., 1998. Adaptive wall techniques. AGARD AG 336.

Zimmermann, N.H., Weissenburger, J.T., 1964. Prediction of flutter onset speed based on flight testing at subcritical speeds. Journal of Aircraft 1, 190–202.

Zwaan, R.J., 1979. Summary of data required for the AGARD SMP activity "Standard Aeroelastic Configurations"—two-dimensional configurations. NLR MP 79015 U.